ELSEVIER

Error modelling, calibration and analysis of an AM–CW terrestrial laser scanner system

Derek D. Lichti *

Department of Spatial Sciences, Curtin University of Technology, GPO Box U1987, Perth, WA 6845, Australia

Abstract

A rigorous method for terrestrial laser scanner self-calibration using a network of signalised points is presented. Exterior orientation, object point co-ordinates and additional parameters are estimated simultaneously by free network adjustment. Spherical co-ordinate observation equations are augmented with a set of additional parameters that model systematic errors in range, horizontal direction and elevation angle. The error models include both physically interpretable and empirically identified components. Though the focus is on one particular make and model of AM–CW scanner system, the Faro 880, the mathematical models are formulated in a general framework so their application to other instruments only requires selection of an appropriate set of additional parameters. Results from controlled testing show that significant improvement is achieved by using the proposed model in terms of both reducing the magnitude of observational residuals as well as the three-dimensional positioning accuracy of signalised points. Ten self-calibration datasets captured over the course of 13 months are used to examine short- and long-term additional parameter stability via standard hypothesis testing techniques. Detailed investigations into correlation mechanisms between model parameters accompany the self-calibration solution analyses. Other contributions include an observation model for incorporation of integrated inclinometer observations into the self-calibration solution and an effective a priori outlier removal method. The benefit of the former is demonstrated to be reduced correlation between exterior orientation and additional parameters, even if inclinometer precision is low. The latter is arrived at by detailed analysis of the influence of incidence angle on range.

1. Introduction

1.1. Background and motivation

Attention to the problem of terrestrial laser scanner (TLS) calibration and validation by the photogrammetry and surveying communities has increased in the last few years. Whilst the need for calibration is obvious to professionals in those disciplines, it is perhaps more urgent given the significant growth in TLS use, particularly by 'non-experts' from other fields. Much of the preliminary work in this area has necessarily been performance evaluation by comparing range measurements or Cartesian co-ordinates rather than spherical co-ordinate observables. A logical outcome of the former was the rangefinder calibration over a baseline. While the latter method can demonstrate the existence of systematic errors, gaining insight into the exact nature and cause of the errors can be difficult. Some of the works in this area

---

* Tel.: +61 8 9266 2691; fax: +61 8 9266 2703.
  E-mail address: d.lichti@curtin.edu.au.

includes Böhler et al. (2003), Hebert and Krotkov (1992), Kersten et al. (2004), Langer et al. (2000), Lichti et al. (2000, 2002) and Schulz and Ingensand (2004a,b).

Among the first in the photogrammetry/surveying community to report on TLS calibration were Rietdorf et al. (2003) and Gielsdorf et al. (2004), who present point-on-plane-condition models and a procedure for self-calibration of the low-cost TLS that they constructed. Their additional parameter (AP) set includes terms for trunnion axis error, vertical index error, horizontal collimation error, additive rangefinder constant and eccentricity. They discuss their use of planar targets rather than point targets and some aspects of their network design. Some advantages of the planar target approach include its system independence (in terms of software and target compatibility) and very high redundancy. They report significant systematic error parameters that are precisely resolved thanks to the redundancy.

Amiri Parian and Grün (2005) exploit some of the common properties shared by panoramic cameras and TLSs. They report the use of 2D image point observations derived from the scanner data in an extended panoramic camera model calibration of the Z+F Imager 5003. Their residual analyses and accuracy assessment demonstrate considerable improvement as result of their modelling. However, there are at least two drawbacks to their approach. First, they only model angular systematic errors, not rangefinder errors. Second, the panoramic-camera model and derived pseudo-observations do not truly represent the geometry of point cloud acquisition, which could make inferring the exact physical nature of systematic error sources difficult.

Lichti and Franke (2005) approach the problem by recognising similarities between theodolites and TLSs, reporting up to 73% improvement in the RMS of residuals for the iQsun 880 (now Faro 880) laser scanner as a result of the modelling. They form spherical observation equations to model the point cloud acquisition geometry and present a seven-term AP error model and free network and self-calibration procedure. Lichti and Licht (2006) report extensions to this model and a set of independent experiments for assessment of various system components. Like Amiri Parian and Grün (2005), they use a point target approach. Similarly, Abmayr et al. (2005) address calibration of the Z+F Imager 5003 with error models originating from theodolite modelling. They propose a simple, non-simultaneous calibration method for estimating trunnion axis error, collimation axis error and vertical circle index error. Reshetyuk (2006) reports self-calibration experiments with both four- and five-term error models conducted on three scanners (Callidus 1.1, Leica HDS 3000 and Leica HDS 2500) but with a limited number of object points (up to 23).

Laser tracker systems share some salient properties with TLSs, so some aspects of their error models and calibration procedures are relevant. Many laser tracker systematic error sources are listed – unfortunately without models – in UCL (2001a). Some range-observation error models (additive constant and scale factor) are given in UCL (2001b), but none are given for angular measurements. Laser tracker system calibration has received considerable attention in robotics, where the ray tracing equations expressed in terms of homogeneous co-ordinates tend to be preferred to the collinearity approach of photogrammetry. Lin and Lu (2005) describe a four-parameter (i.e. not-full system) laser tracker calibration which includes terms for offsets in the rotating mirror mechanisms. Spiess et al. (1998) discuss laser tracker construction and procedures for system calibration, one of which uses the familiar direct- and reverse-scope angle readings. Zhuang and Roth (1995) present models for gimbal axis misalignment and mirror centre offset in a laser tracker and a system calibration procedure. Li and Mitchell (1995) also present a model for scanning mirror surface offset along with a method for its calibration for a scanning laser Doppler vibrometry system.

1.2. Paper outline

In this paper the full mathematical model for a point-based, photogrammetric approach to TLS self-calibration is presented. This commences with the models for spherical co-ordinate observations and scanner inclinometer observations. Next, the models for physical and empirically determined systematic errors are proposed and explained with examples to justify model choice where necessary. Though the focus of this paper is on one particular make and model of amplitude-modulated−continuous-wave (AM−CW) TLS system, the underlying mathematical models are derived independently of a particular instrument and can therefore be easily modified to suit others. Furthermore, the need for TLS calibration in other instrument makes is well established by results from other researchers, as indicated earlier. Presentation of the structure of relevant least-squares matrix equations and discussion of applicable datum constraints complete the mathematics. Results and analyses from 10 highly redundant self-calibration datasets captured over a 13-month period then follow. The results of implementing the proposed AP model are examined both in terms of improvements to the self-calibration residuals and through independent accuracy assessment. Additional parameter significance and both short-term and long-term AP stability are then analysed. It will also be shown that the range

observations are significantly influenced by the incidence angle at which a target is scanned. The outcome of this is a pre-adjustment outlier removal procedure. Finally, the effects of the inclinometer observations are investigated. The benefits of doing so are shown to be considerable in terms of reducing parameter correlation despite the low inclinometer precision.

2. Mathematical models

2.1. Observation equations

The rigid-body transformation of point i from object space to scanner space j, in which the observations are made, is given by

$$
\begin{bmatrix} x_{ij} \\ y_{ij} \\ z_{ij} \end{bmatrix} = R_3(\kappa_j)R_2(\phi_j)R_1(\omega_j) \left\{ \begin{bmatrix} X_i \\ Y_i \\ Z_i \end{bmatrix} - \begin{bmatrix} X_{s_j} \\ Y_{s_j} \\ Z_{s_j} \end{bmatrix} \right\}
$$

$$
= M_j \left\{ \begin{bmatrix} X_i \\ Y_i \\ Z_i \end{bmatrix} - \begin{bmatrix} X_{s_j} \\ Y_{s_j} \\ Z_{s_j} \end{bmatrix} \right\} \qquad (1)
$$

where

(X_s, Y_s, Z_s) are the object space co-ordinates of scanner position j;

(ω, ϕ, κ) are the Cardan angles (ω, ϕ, κ) for the rotation from object space to scanner space j;

(X, Y, Z) are the object space co-ordinates of object point i;

(x, y, z) are the co-ordinates of object point i in scanner space j;

R_1, R_2, R_3 are the matrices for rotation about the X-, Y- and Z-axes, respectively.

The parameters (X_s, Y_s, Z_s) and (ω, ϕ, κ) constitute the exterior orientation (EO) elements of scan location j. Since Cartesian co-ordinates are derived quantities, the more favourable geometric parameterisation is in terms of the basic observation of range, ρ, horizontal direction, θ, and elevation (vertical) angle, α,

$$
\rho_{ij} + v_{\rho_{ij}} = \sqrt{x_{ij}^2 + y_{ij}^2 + z_{ij}^2} + \Delta\rho \qquad (2)
$$

$$
\theta_{ij} + v_{\theta_{ij}} = \arctan\left(\frac{y_{ij}}{x_{ij}}\right) + \Delta\theta \qquad (3)
$$

$$
\alpha_{ij} + v_{\alpha_{ij}} = \arctan\left(\frac{z_{ij}}{\sqrt{x_{ij}^2 + y_{ij}^2}}\right) + \Delta\alpha \qquad (4)
$$

where v in each equation represents the respective residual. Substitution of the relevant terms of Eq. (1) into these completes the observation equations. Eqs. (2)–(4) are augmented with respective systematic error correction models, $\Delta\rho$, $\Delta\theta$ and $\Delta\alpha$, which are described in the next section. These constitute the interior orientation (IO) of the scanner and are assumed to be block-invariant for the purpose of self-calibration.

If the scanner is level, which is possible when it is fitted with two orthogonal inclinometers, two parameter observations can be written for each scan location

$$
\omega_j + v_{\omega_j} = 0 \qquad (5)
$$

$$
\phi_j + v_{\phi_j} = 0 \qquad (6)
$$

The instrument under investigation here, the Faro 880, possesses inclinometers. More details about their function for the are given in Section 3.1 and the benefits of incorporating these observations into the self-calibration solution are analysed in detail in Section 4.5.

2.2. Systematic error models

The AP models are classified into two groups. The first is the set of physical parameters that form what might be considered a basic AP set. TLSs have several salient properties in common with total stations so many of the physical models can be drawn from the relevant foundation literature (e.g., Cooper, 1982; Rüeger, 1990). This group includes the rangefinder additive constant, cyclic errors, collimation and trunnion axis errors, vertical circle index error and others that are fully described herein. The second group is the empirical parameters whose physical cause is not necessarily apparent and may be due to geometric defects in construction and/or electrical cross-talk and may be system-dependent. These are generally sinusoidal as functions of horizontal direction or elevation angle. They were determined in this study by exploratory data analyses of the residuals from highly redundant self-calibration adjustments of the many available datasets. The choice of appropriate models to remove the discovered trends was governed by function simplicity (e.g., sinusoids), which in many cases resulted in low correlation with other estimable parameters, and the desire to minimise the number of parameters required. The current AP model for the Faro 880 consists of 17 coefficients, each of which is explained in more detail below. Coefficients are numbered according to the chronology of their addition to the model and the reasons for terms omitted from the series are given. Residual plots showing the trend to be modelled are provided for some

model terms; plots for others can be found in Lichti and Franke (2005) and Lichti and Licht (2006).

2.2.1. Range APs

The rangefinder AP model comprises 9 coefficients as shown in Eq. (7). The rangefinder additive correction is modelled as a constant, a_0, and applies to the Faro 880 instrument/planar-target combination used herein (Witte and Schwarz, 1982). Though this is a rather fundamental concept, it is worth noting again particularly in light of the work of Kersten et al. (2005) with the Mensi GS100. Their baseline testing of this instrument's rangefinder revealed a 15 mm mean difference between distances derived from planar targets and those of spherical targets, though they indicate this may be due to the software algorithms used. The cyclic error terms inherent to AM–CW rangefinder systems are represented by a_3 and a_4. In the Faro 880 system they have been found to exist with a period of 0.6 m, which is half of the finest unit length, U_1. Rüeger (1990) calls these the second-order short periodic errors. Both Langer et al. (2000) and Ingensand (2006) demonstrate the existence of cyclic errors in Z+F scanners with both long- (on the order of tens of metres) and short-wavelength (on the order of metres) components. Experience calibrating the Faro instrument has found, on one occasion, cyclic errors with a period of 4.8 m, which equals one-half the median unit length, U_2. Though precedence for the existence of such errors exists elsewhere in the literature (Covell and Rüeger, 1982), these terms, a_5 and a_6, are omitted from the final model due to the lack of repeatable

trend in the range residuals (as opposed to statistical repeatability of the APs). Scale, a_1, is also omitted from the model since its estimation requires inclusion of an independent scale definition in the self-calibration network. Furthermore, independent baseline testing did not reveal the existence of this error (Lichti and Licht, 2006). Though the software developed in support of this work does allow inclusion of independent distance observations, none are included in any of the experimental datasets.

$$\Delta\rho = a_0 + a_1\rho_{ij} + a_2\sin(\alpha_{ij}) + a_3\sin\left(\frac{4\pi}{U_1}\rho_{ij}\right)$$
$$+ a_4\cos\left(\frac{4\pi}{U_1}\rho_{ij}\right) + a_5\sin\left(\frac{4\pi}{U_2}\rho_{ij}\right)$$
$$+ a_6\cos\left(\frac{4\pi}{U_2}\rho_{ij}\right) + a_7\sin(4\theta_{ij}) + a_8\cos(4\theta_{ij})$$
$$(7)$$

The sinusoidal error in range, a_2, has a 360° period and is hypothesised to be due to a vertical offset between the laser and trunnion axes. It is zero for horizontal elevation angles (i.e. 0° and 180°) and reaches a maximum at the instrument's zenith. Though simulation confirmed this as a plausible physical cause (Lichti and Franke, 2005), it is still regarded an empirical parameter. The terms a_7 and a_8 model a sinusoidal error in range as a function of horizontal direction with period 90°, for which the physical cause is not known. Fig. 1 (Top) shows the self-calibration residuals from the first 28 October 2005 dataset (details of the
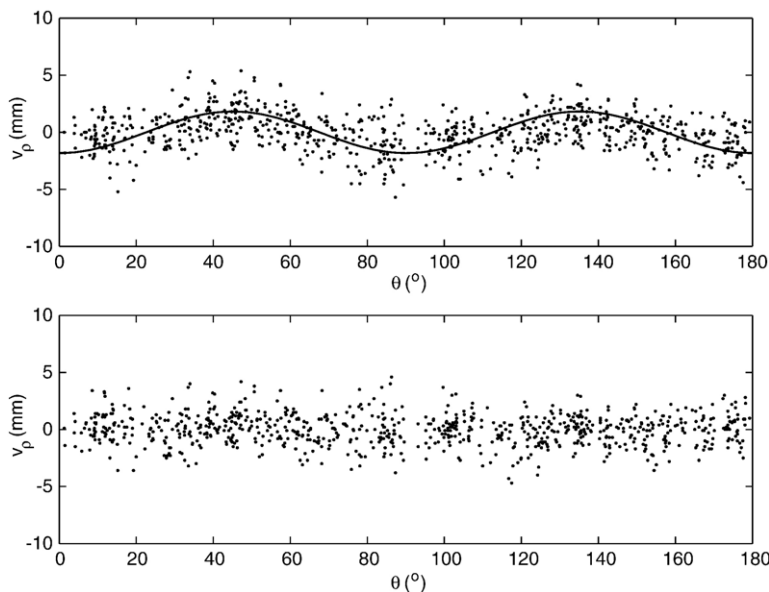

Fig. 1. Range residuals as a function of horizontal direction for the first 28 October 2005 dataset (calibration 7). Top: without a_7 and a_8 and estimated correction model. Bottom: with a_7 and a_8.

Table 1
Self-calibration summary and results for all 10 datasets

	Calibration dataset									
	1	2	3	4	5	6	7	8	9	10
	10 December 2004	31 March 2005	7 June 2005	8 August 2005	9 August 2005	27 September 2005	28 October 2005 (1)	28 October 2005 (2, Faro parameters set to zero)	7 December 2005	19 January 2006
Number of targets	181	130	148	62	62	63	134	133	131	135
Redundancy	2803	2218	1894	835	832	931	2008	2017	1741	1638
Room dimensions (m)	$12 \times 9 \times 3$	$12 \times 9 \times 3$	$9 \times 5 \times 3$	$9 \times 5 \times 3$	$9 \times 5 \times 3$	$9 \times 5 \times 3$	$9 \times 5 \times 3$	$9 \times 5 \times 3$	$12 \times 9 \times 3$	$12 \times 9 \times 3$
Without APs										
RMS ρ (mm)	±2.4	±2.1	±2.3	±2.4	±2.2	±2.4	±2.5	±2.7	±2.3	±3.2
RMS θ (″)	±99	±67	±76	±87	±106	±140	±93	±197	±126	±68
RMS α (″)	±35	±46	±26	±18	±22	±54	±45	±75	±52	±54
With APs										
RMS ρ (mm)	±1.1	±1.2	±1.1	±1.2	±1.1	±1.7	±1.4	±1.2	±1.2	±1.8
RMS θ (″)	±18	±12	±18	±25	±22	±22	±19	±17	±26	±21
RMS α (″)	±17	±22	±14	±12	±11	±13	±11	±12	±14	±29
% Improvement										
RMS ρ	54	43	52	50	50	29	44	56	48	44
RMS θ	82	82	77	72	80	85	80	91	79	69
RMS α	51	52	46	32	50	76	75	85	72	47

datasets are given in Section 3.2 and are summarised in Table 1) without inclusion of these two terms and the estimated error model. Note that the horizontal direction range of [0°, 180°] is due to the Faro instrument's mode of operation, which is explained in detail in Section 3.1. Fig. 1 (Bottom) shows the residuals after their inclusion. Clearly, they are effective in removing the trend.

2.2.2. Horizontal direction APs

The seven-term horizontal direction AP model is given by Eq. (8). Two of the largest angular error sources are the collimation axis error, b_1, and trunnion axis error, b_2, which respectively vary with the secant and the tangent of elevation angle. Their models given here differ from those of Abmayr et al. (2005) due to the different parameterisation
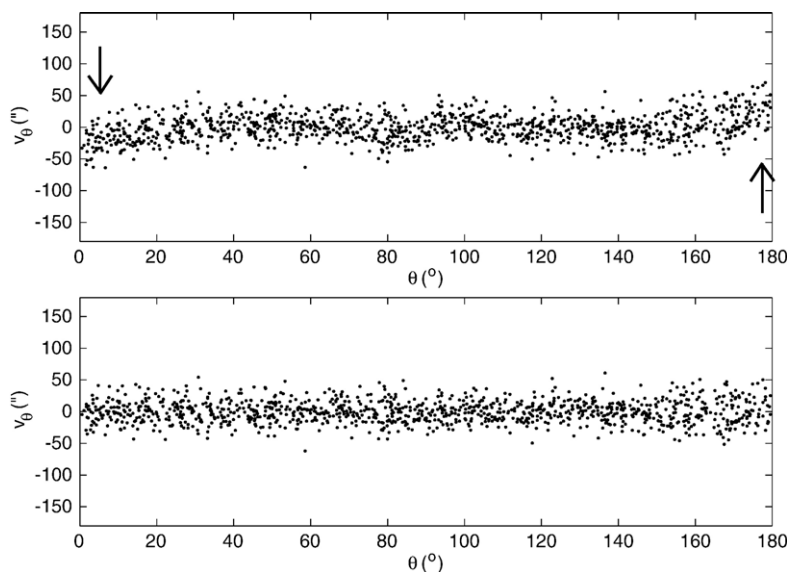

Fig. 2. Horizontal direction residuals as a function of horizontal direction for the 10 December 2004 dataset (calibration 1). Top: without b_5. Bottom: with b_5.

of elevation angle. The non-orthogonality of the plane containing the horizontal angle encoder and the vertical axis causes a sinusoidal error with period 180° and is modelled by the coefficients b_3 and b_4. The b_5 term models a scale error in horizontal direction. As can be seen for the 10 December 2004 dataset in Fig. 2, this error does not explicitly manifest itself as a linear trend in the direction residuals. Instead, it biases the estimation of b_3 and b_4, from which the resulting residual pattern is a tilted sinusoid with period 180°. This effect can be best seen at the tails of the residuals indicated by the arrows in Fig. 2 (Top). At 0°, the tail is negative and at 180° the tail is positive. A complete error model might also include two additional coefficients for horizontal circle eccentricity, for which the effect is sinusoidal with period 360°. These have been excluded simply because they were not found to be necessary for any of the datasets captured thus far. However, significant vertical circle eccentricity has been found, as described in the next subsection.

$$\Delta\theta = b_1 \sec(\alpha_{ij}) + b_2 \tan(\alpha_{ij}) + b_3 \sin(2\theta_{ij})$$
$$+ b_4 \cos(2\theta_{ij}) + b_5 \theta_{ij} + b_6 \cos(3\alpha_{ij}) + b_7 \sin(4\alpha_{ij}) \tag{8}$$

The empirical terms b_6 and b_7 model residual errors in horizontal direction as a function of elevation angle that are not corrected by the collimation axis and trunnion axis models. Their effect is most significant at high elevation angles and their source may be wobbling of the trunnion axis, which Harvey and Rüeger (1992) note can be modelled as a Fourier series, as has been done here. As an example, Fig. 3 (Top) pictures the trend in the 7 December 2005 dataset before inclusion of b_6 with superimposed error model trend. Fig. 3 (Bottom) shows the residuals after inclusion of b_6. To illustrate their need, consider the following three calibration examples chosen at random: 10 December 2004, 31 March 2005 and 7 June 2005. Without the b_6 term, the numbers of outliers identified by Baarda's data snooping after self-calibration are 48, 24 and 10, respectively. Without b_7, the respective numbers are 4, 6 and 4, which are lower but nonetheless outliers due to unmodelled systematic error.

2.2.3. Elevation angle APs

The elevation angle correction model is given by Eq. (9). The first term is the well-known vertical circle index error, c_0. Scale in elevation angle, c_1, was implemented at the same time as was the horizontal direction scale, b_5, but is omitted from the final model since it is nearly perfectly correlated to c_0 and there was no evidence in the residuals to suggest it was needed. The reason for the high correlation is not clear, though, since a good distribution of elevation angle observations existed in every calibration dataset. Addition of the scale term to the model also resulted in very high correlations (i.e. >0.95) between c_0 and c_1 and certain EO elements, namely Z_s and ω, which suggests the functional dependence is more complex. The c_2 term models a sinusoidal error in elevation angle with a period of 360°, which suggests circle
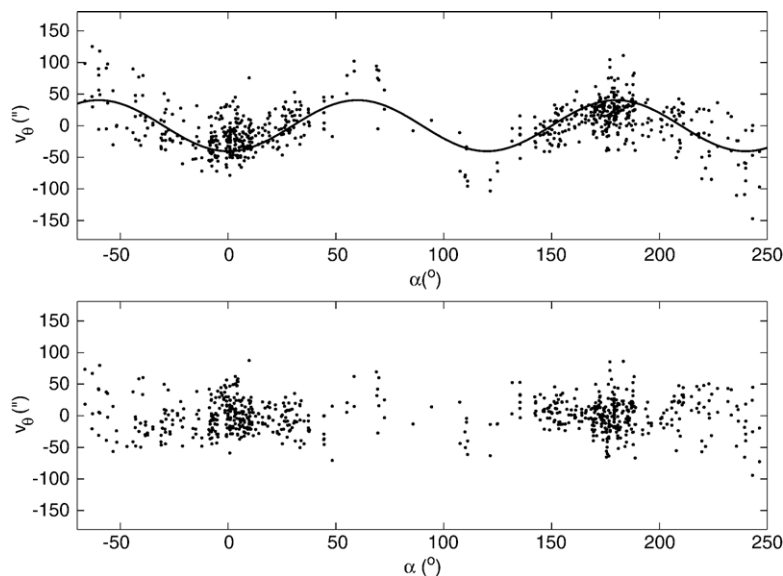

Fig. 3. Horizontal direction residuals as a function of elevation angle for the 7 December 2005 dataset (calibration 9). Top: without b_6 and estimated correction model. Bottom: with b_6.

eccentricity error. Only the sine coefficient is included in the model since the cosine term is nearly perfectly correlated to certain positional and rotational elements of the exterior orientation and, therefore, omitted.

$$\Delta\alpha = c_0 + c_1\alpha_{ij} + c_2\sin(\alpha_{ij}) + c_3\sin(3\theta_{ij}) + c_4\sin(3\theta_{ij}) \tag{9}$$

The empirical c_3 and c_4 terms model a sinusoidal error a function of horizontal direction with period of 120°. The residuals for the 31 March 2005 dataset without these terms along with the estimated error model are plotted in Fig. 4 (Top) and residuals after their inclusion are given in Fig. 4 (Bottom). One possible cause of this error is mechanical wobble of the instrument in its tribrach as it rotates about its vertical axis, as Kersten et al. (2005) found for a Mensi laser scanner. The scanner studied herein has been consistently observed to go slightly off level (as indicated by the tribrach's bull's eye bubble) upon completion of the 180° horizontal scan, so this is indeed a plausible cause.

2.3. Model adaptation to other sensors

The basic modelling approach presented herein is for time-of-flight scanning systems but is designed to be independent of both the type of rangefinder and the deflection mechanism used by a particular instrument. The range observation model is applicable to both pulse and AM–CW rangefinders. From a mathematical modelling perspective, the differences between the range observables of the methods lie in the systematic error terms which are easily added

or removed from the model. For example, the cyclic error parameters would not be included in the AP model for a pulse system since they are only relevant to AM–CW systems.

Several methods of beam deflection exist, including rotating polygonal mirrors, rotating monogonal mirrors and galvanometers (nodding mirrors). The horizontal direction and elevation angle observation equations are expected to be applicable to each of these. The main differences lie in the allowable range for each angle observable, which depends upon the field of view of a particular instrument, and the error modelling. In case of the polygonal mirror scanners, for example, a systematic range error is known to exist due to the offset of the of the mirror surface from the rotation axis (e.g., Riegl, 2001). However, this can easily be accommodated by adding an appropriate error model. In principle this error does not exist for monogonal scanners such as the Faro 880.

2.4. Adjustment model

The five groups of observations (Eqs. (2)–(6)) can be arranged in (linearised) hyper-matrix form as follows

$$\begin{bmatrix} A_{\rho e} & A_{\rho a} & A_{\rho o} \\ A_{\theta e} & A_{\theta a} & A_{\theta o} \\ A_{\alpha e} & A_{\alpha a} & A_{\alpha o} \\ A_{\omega e} & 0 & 0 \\ A_{\phi e} & 0 & 0 \end{bmatrix} \begin{bmatrix} \hat{\delta}_e \\ \hat{\delta}_a \\ \hat{\delta}_o \end{bmatrix} + \begin{bmatrix} w_\rho \\ w_\theta \\ w_\alpha \\ w_\omega \\ w_\phi \end{bmatrix} = \begin{bmatrix} \hat{v}_\rho \\ \hat{v}_\theta \\ \hat{v}_\alpha \\ \hat{v}_\omega \\ \hat{v}_\phi \end{bmatrix} \tag{10}$$

where A_{xy} represents the Jacobian (design) matrix of partial derivatives of an observation group x (ρ, θ, α, ω
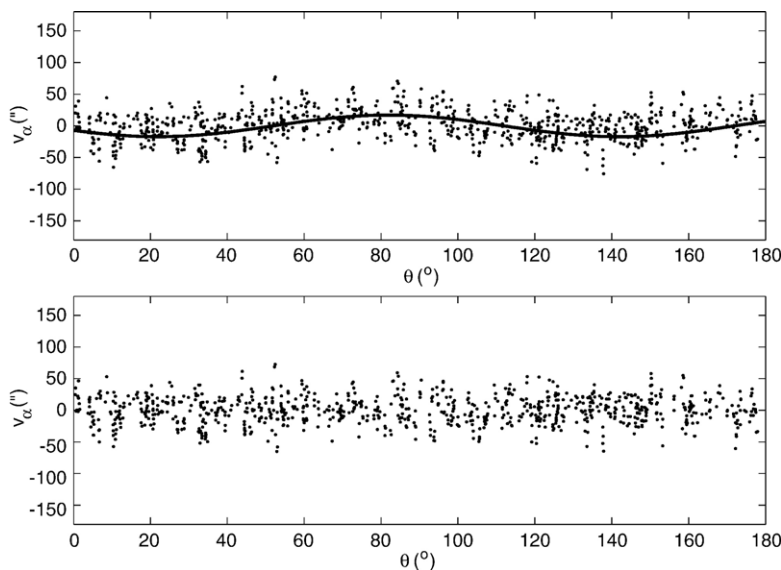

Fig. 4. Elevation angle residuals as a function of horizontal direction for the 31 March 2005 dataset (calibration 2). Top: without c_3 and c_4 and estimated correction model. Bottom: c_3 and c_4.

or ϕ) taken with respect to parameter set y (e, a or o, which refer to the parameter sets for the EO, APs and object point co-ordinates, respectively); δ_y represents the vector of corrections to the approximate values for parameter set y; and w_x and v_x are the misclosure vector (calculated minus observed values) and estimated residuals, respectively, for observation group x. The ^ indicates an estimable quantity.

The total number of observations, n, is simply three times the number of scanned points plus, if the inclinometer observations are available, two times the number of scans. The total unknowns is given by

$$u = u_e + u_o + u_a \qquad (11)$$

where u_e is the number of scanner orientation parameters, equal to 6 times the number of scan locations; u_o is the number of object point parameters, equal to 3 times the number of object points; and u_a is the number of APs in the IO error models. The total degrees of freedom are

$$r = n - u + d \qquad (12)$$

where d is the number of datum constraints. Without inclinometer observations, d is 6 since 3 translation and 3 rotation datum defects are undefined. Scale is defined implicitly by the range observations. If available, the inclinometer observations remove the rotation defects about the X- and Y-axes, in which case d is 4. The inner constraints imposed on object points to remove the datum defects are given in matrix form by

$$\begin{bmatrix} 0 & 0 & G_o^T \end{bmatrix} \begin{bmatrix} \hat{\delta}_e \\ \hat{\delta}_a \\ \hat{\delta}_o \end{bmatrix} = [0] \qquad (13)$$

The analytical form of the datum constraint design matrix, G_o, is standard and can be found in Kuang (1996), for example.

Weights are assumed to be inversely proportional to variance and are assigned on a group-wise basis so the weight matrix, **P**, is block diagonal

$$\mathbf{P} = \begin{bmatrix} P_\rho & 0 & 0 & 0 & 0 \\ 0 & P_\theta & 0 & 0 & 0 \\ 0 & 0 & P_\alpha & 0 & 0 \\ 0 & 0 & 0 & P_\omega & 0 \\ 0 & 0 & 0 & 0 & P_\phi \end{bmatrix} \qquad (14)$$

Observational errors are assumed to be uncorrelated to those within the same group as well as those of other

groups. The bordered system of normal equations follows from standard parametric least squares and is given by

$$\begin{bmatrix} \begin{pmatrix} A_{\rho e}^T P_\rho A_{\rho e} \\ +A_{\theta e}^T P_\theta A_{\theta e} \\ +A_{\alpha e}^T P_\alpha A_{\alpha e} \\ +A_{\omega e}^T P_\omega A_{\omega e} \\ +A_{\phi e}^T P_\phi A_{\phi e} \end{pmatrix} & \begin{pmatrix} A_{\rho e}^T P_\rho A_{\rho a} \\ +A_{\theta e}^T P_\theta A_{\theta a} \\ +A_{\alpha e}^T P_\alpha A_{\alpha a} \end{pmatrix} & \begin{pmatrix} A_{\rho e}^T P_\rho A_{\rho o} \\ +A_{\theta e}^T P_\theta A_{\theta o} \\ +A_{\alpha e}^T P_\alpha A_{\alpha o} \end{pmatrix} & 0 \\ & \begin{pmatrix} A_{\rho a}^T P_\rho A_{\rho a} \\ +A_{\theta a}^T P_\theta A_{\theta a} \\ +A_{\alpha a}^T P_\alpha A_{\alpha a} \end{pmatrix} & \begin{pmatrix} A_{\rho a}^T P_\rho A_{\rho o} \\ +A_{\theta a}^T P_\theta A_{\theta o} \\ +A_{\alpha a}^T P_\alpha A_{\alpha o} \end{pmatrix} & 0 \\ & & \begin{pmatrix} A_{\rho o}^T P_\rho A_{\rho o} \\ +A_{\theta o}^T P_\theta A_{\theta o} \\ +A_{\alpha o}^T P_\alpha A_{\alpha o} \end{pmatrix} & G_o \\ \text{sym.} & & & 0 \end{bmatrix} \begin{bmatrix} \hat{\delta}_e \\ \hat{\delta}_a \\ \hat{\delta}_o \\ \mathbf{k}_c \end{bmatrix}$$

$$+ \begin{bmatrix} \begin{pmatrix} A_{\rho e}^T P_\rho w_\rho \\ +A_{\theta e}^T P_\theta w_\theta \\ +A_{\alpha e}^T P_\alpha w_\alpha \\ +A_{\omega e}^T P_\omega w_\omega \\ +A_{\phi e}^T P_\phi w_\phi \end{pmatrix} \\ \begin{pmatrix} A_{\rho a}^T P_\rho w_\rho \\ +A_{\theta a}^T P_\theta w_\theta \\ +A_{\alpha a}^T P_\alpha w_\alpha \end{pmatrix} \\ \begin{pmatrix} A_{\rho o}^T P_\rho w_\rho \\ +A_{\theta o}^T P_\theta w_\theta \\ +A_{\alpha o}^T P_\alpha w_\alpha \end{pmatrix} \\ 0 \end{bmatrix} = \begin{bmatrix} 0 \\ 0 \\ 0 \\ 0 \end{bmatrix} \qquad (15)$$

where $\mathbf{k}_c$ is the vector of Lagrange multipliers.

3. Experiments

3.1. Faro Instrument

Pictured in Fig. 5, the Faro 880 terrestrial laser scanner offers a near-spherical field of view made possible by a 320° (−70° to 250°) vertical angle scanning range and a 180° horizontal field of view. The former is possible due to the monogon beam deflection mechanism. The AM–CW rangefinder operates by the phase difference method in which the (ambiguous) range is proportional to the phase difference between the received and emitted signals (Rüeger, 1990). Three unit lengths are used: the shortest is nominally 1.2 m and the other two differ by factors of 8, nominally 9.6 m and 76.8 m. In terms of rangefinder performance, the manufacturer specifies that the (systematic) linearity error in the rangefinder is ≤ 3 mm at a range of 10 m and 84% surface reflectivity. For more recent incarnations of the system, though, the 3 mm linearity error is specified at 20 m for a stationary target at orthogonal incidence. Linearity error is caused by the non-linear relationship between system output voltage, which is proportional to the observed phase difference, and range. It is inherent to the amplification circuits of

Fig. 5. The Faro 880 terrestrial laser scanner.

the rangefinder; Adams (1999) gives a full account of its cause and effect.

For the particular instrument studied, no further performance data were available from the manufacturer. However, more specifications are available for newer incarnations of the 880 system, which are presented here for indicative purposes only. In terms of rangefinder repeatability for the more recent system, the manufacturer specifies ±2.6 mm and ±5.2 mm for 90% and 10% reflectivity, respectively, at 10 m range. At 25 m range, the repeatability for 90% is ±4.2 mm and is ±10 mm for 10%. Angular precision for the newer instrument is quoted as ±0.009° (±32″).

The scanner features two orthogonal inclinometers that measure instrument tilt. Their outputs are used by the software to correct the captured scan data resulting in a 'levelled' dataset, which justifies the use of Eqs. (5) and (6) for zero-valued ω and ϕ angles. The software capability for the levelling by inclinometer measurement only became available toward the end of the 13-month study period, though: after the September 2005 servicing. The manufacturer specifies ±0.01° (±36″) for the inclinometer accuracy.

3.2. Self-calibration experiments

A similar procedure was followed for 10 calibrations of a Faro 880 scanner conducted over the course of 13 months with the first and last tests conducted on 10 December 2004 and 19 January 2006, respectively. Hereafter these datasets will be referred to by calibration number (1 to 10)—see Table 1 for the date of each. An array of a varying number of proprietary Faro targets

was set up in an indoor laboratory. Planar, A4-size Faro targets mounted on a rigid backing were affixed to the four walls, floor and ceiling. Smaller, A5-size targets were used only for calibration 1. Two different rooms were available: $12 \times 9 \times 3$ m used for calibrations 1, 2, 9 and 10; and a smaller $9 \times 5 \times 3$ m room for the rest. The room and Faro targets used for calibration 2 are pictured in Fig. 6. Eight scans of the target array were captured for each: four from each of two nominal locations, except in one instance. The instrument was manually rotated atop the tripod by 90° after each scan was captured. For calibration 10, two scans from 4 locations were instead captured. In all cases the height of instrument was midway between floor and ceiling.

Datasets 4 and 5 were captured to examine short-term AP stability. In the day between these two data-capture sessions, the instrument was put away in its rugged case. Between other calibration dates the scanner was used a considerable amount and shipped by air a number of times. Datasets 7 and 8 were captured on the same day: one under normal operating conditions and the other with selected Faro calibration parameters set to zero to examine the effect of doing so. The instrument was not put away between capture of datasets on this occasion. Results from this test concerning the nature of the selected Faro parameters and the resulting impact on b_1 (collimation axis error) and b_2 (trunnion axis error) are reported in Lichti and Licht (2006). Also noteworthy is that the instrument was serviced prior to calibration 6 and it experienced a minor shock load prior to calibration 10.

In each case scan resolution was set in the iQscene controlling software to the 1/4 option, for which the angular sampling interval is 0.044°. Higher resolution scans were not possible due to memory limitations of the

Fig. 6. View of room and Faro targets used for the 31 March 2005 dataset (calibration 2).

controlling laptop computer. The linear sampling increment at the selected resolution was 7.7 mm at 10 m range, so the number of samples across the target diameter at normal incidence at this range was 19 for the A4-size target and 13 for the A5. Horizontal and vertical scan extents were set to the maximum values described earlier. Room temperature on all occasions was controlled and was measured to be 22 °C or 23 °C. Lighting conditions were also the same: overhead fluorescent lighting with some indirect solar light through louver-shaded windows. Target centre measurement was performed using the "contrast centroiding" tool within iQscene, the performance of which in range is reported in Lichti and Licht (2006). iQscene permits the export of scanner space, Cartesian co-ordinates. These have been corrected for systematic errors – though not completely, as has been demonstrated in Figs. 1–4 and is indicated by the need for 17 APs – using manufacturer-determined parameters, the models for which are unpublished. Spherical co-ordinate observations must be derived from these Cartesian co-ordinates according to Eqs. (2), (3) and (4) subject to the aforementioned constraints of the allowable ranges for the angles governed by the instrument scanning extents. The self-calibration adjustment of each dataset was performed using software composed by the author.

Several important aspects of the network design are worthy of discussion. First, a large elevation angle range was needed for estimation of the collimation axis and trunnion axis errors. For the 10 datasets it ranged from 122° to 152° thanks to the targets on the floor and ceiling. At least two locations and a variety of ranges were needed for rangefinder additive constant determination. A large variety of ranges was also needed to estimate cyclic errors. From sampling theory, 0.3 m is the required minimum sampling interval for recovery of the 0.6-m-period cyclic error, though a much higher rate is desired and was achieved. The minimum range varied from 1.4 m to 1.8 m (1.5 m is the suggested minimum operating range) while the maximum range depended upon the room used and ranged from 7.3 m to 10.3 m.

Orthogonal scans captured from the same nominal location, a technique borrowed from photogrammetric camera calibration, was an additional measure incorporated to de-correlate the EO and the APs. High redundancy, and therefore a large number of targets, was desired so that trends in residual plots uncovered during the exploratory data analyses could be safely hypothesised to be due to un-modelled systematic errors. Table 1 gives the number of object points and redundancy

for each dataset, along with some of the self-calibration results discussed in the following section.

4. Analyses of results

4.1. Model efficacy

Table 1 gives the RMS of residuals both with and without APs as well as the resulting per cent improvement for each of the self-calibration datasets. It is clear from the figures in Table 1 that great benefit was realised as a result of applying the proposed AP model since the mean improvements in residual RMS are 47%, 79% and 59% for range, horizontal direction and elevation angle, respectively. The respective overall RMS estimates calculated from the combined results of the 10 datasets without APs are ±2.5 mm, $\pm112''$ and $\pm45''$, and with APs are ±1.3 mm, $\pm20''$ and $\pm17''$. No dependence of the RMS in either variable exists as a function of time or adjustment redundancy was found (though the horizontal direction values are more variable), so these would seem to be reasonable estimates of system measurement noise.

Further assessment was possible using 45 independently surveyed points scanned from three separate locations on the same day as calibration 9. The targets were co-ordinated by intersection from two total station instrument locations and a 900 mm Leica scale bar ($\sigma = \pm0.002$ mm) was included in the network for scale definition. The estimated mean co-ordinate precision of the surveyed points was ±0.5 mm in the horizontal and ±0.1 mm in height at 68% confidence. More points than the 45 mentioned were surveyed but many were eliminated *a priori* according to the incidence-angle criterion outlined in Section 4.5. A total of 120 scanner-space point observations were available for the accuracy assessment.

A simultaneous, rigid-body transformation adjustment of the 120 point observations from all 3 scans was performed with the surveyed points defining the inner

Table 2
Accuracy assessment results from the 7 December 2005 dataset (calibration 9)

	Without AP correction	With AP correction	% Improvement
RMS ρ (mm)	±2.8	±1.8	36
RMS θ ($''$)	±44	±31	30
RMS α ($''$)	±23	±16	30
RMS x (mm)	±2.3	±1.8	22
RMS y (mm)	±2.2	±1.6	27
RMS z (mm)	±1.1	±0.6	45

constraints datum. The resulting difference statistics are complied in Table 2 in terms of both spherical and Cartesian co-ordinates. Though the benefit of the AP models can be clearly seen, the effectively uniform ($\geq 30\%$) improvement in spherical co-ordinates is somewhat different than what was consistently achieved from self-calibration. However, the per cent improvement measure is somewhat deceiving in this instance. First, the RMSs of residuals without AP corrections are much lower than the overall values from the 10 calibration datasets without AP correction. This may be due to the more limited network geometry in terms of elevation angle range. Second, the RMSs with AP corrections are commensurate with the overall values from self-calibration for range and elevation angle, with that of horizontal direction being slightly higher at $\pm 31''$. Analyses of the differences plotted as a function of model variables (ρ, θ, α, x, y and z) did not reveal any un-modelled trends. Additionally, the improvement gained by each individual AP (or pair of APs where both sine and cosine terms exist) was assessed by performing the adjustment with the observations corrected only for that particular AP or AP pair. Those that contributed the most to accuracy improvement were a_0, a_2, b_1, b_6, c_0 and c_2.

4.2. Parameter correlation and precision

Most APs in the proposed model are uncorrelated with each other and with the EO parameters; those that are not are analysed here and in Section 4.5. First, the estimation of b_5 (horizontal direction scale factor) is weakened by functional dependence with other parameters, particularly κ and b_3 (coefficient of non-orthogonality between the horizontal circle and vertical axis). The magnitude of the correlation coefficient with the former consistently ranged from 0.7 to 0.8. For the latter the correlation was higher, reaching up to 0.92. It should also be noted that b_3 was correlated to the nearly same degree with κ as was b_5, with coefficients ranging between 0.6 and 0.8. These correlations were independent of degrees of freedom and horizontal angle range, which was always the full 180°.

The two empirical parameters in the horizontal direction model were found to be correlated with other APs: b_6 (periodic error as a function of elevation angle) with b_1 (collimation axis error) by up to 0.80; and b_7 (periodic error as a function of elevation angle) with b_2 (trunnion axis error) by up to 0.57. The latter correlation decreases as the observed elevation angle range (to be interpreted as the range about the horizon) increases, as shown in Fig. 7 (Top). In the worst case (calibration 2), the range was 122° and the correlation coefficient magnitude was 0.57 whereas for calibration 9 the correlation was negligible (0.03) due to the 152° elevation angle range. Surprisingly, no such relationship exists between b_1 and with b_6. Instead, the relative precision between elevation angle and horizontal direction – both of which are weighted on a group-wise basis and optimised using
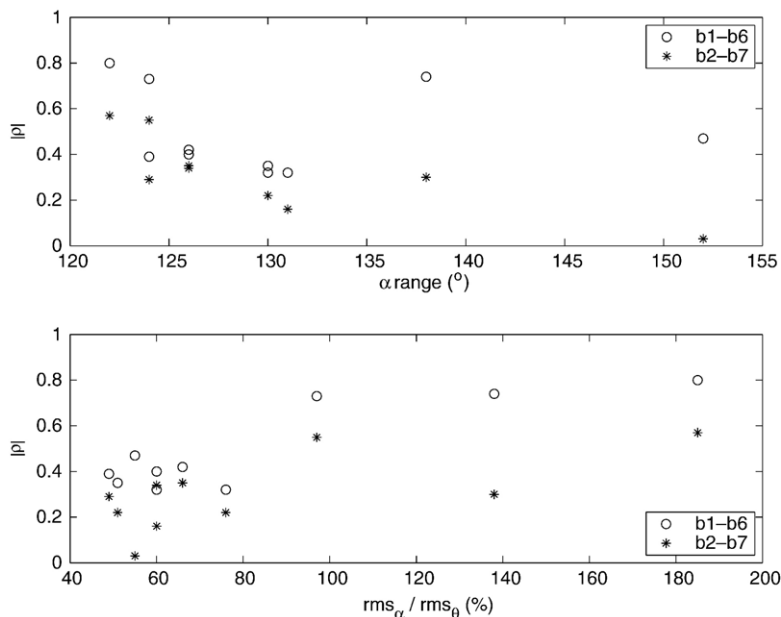

Fig. 7. Top: Correlation coefficient magnitude, $|\rho|$, as a function of elevation angle. Bottom: Correlation coefficient magnitude as a function of the ratio of elevation angle precision to horizontal direction precision.

variance component estimation – was found to be an important factor. When elevation angle was more precise the correlation was low (e.g., correlation of 0.32 for a precision ratio of 51%), but the reverse was true when horizontal direction was more precise (e.g., 0.8 correlation for the ratio of 185%). As shown in Fig. 7 (Bottom), the relationship is not exactly linear, but does show a clear trend. A similar but somewhat weaker dependence exists for the correlation between b_2 and with b_7. Note that observable precision has been quantified in terms of residual RMS rather than *a priori* standard deviation. However, there is little practical difference between the ratios of the former and the latter since variance component estimation was used.

Room size, and therefore maximum range, surprisingly had only a minor influence on the solution quality in terms of the correlation between the additive constant, a_0, and X_s and Y_s scanner position elements of the EO. For the smaller rooms, the magnitude of the maximum correlation coefficient from the 8 scans was 0.86, whereas for the larger rooms it reached only 0.80. Though the availability of longer ranges in a much larger calibration room might very well reduce this correlation further, the angular sampling interval would have to be decreased (thereby increasing data volume) to ensure a sufficient number of returns were received from the targets. The change in network geometry from two nominal locations to four also had only minor impact, reducing the maximum correlation coefficient

magnitude to 0.74. The number of object-space targets, and therefore redundancy, had a similar, minor influence as well.

Overall, estimated AP precision, measured here at 68% confidence (1σ), was very high thanks to the high redundancy and network design measures taken to reduce correlation as much as possible. The greatest precision for the range APs was ±0.1 mm, which was achieved for several parameters. The poorest precision was ±0.4 mm, which was for a_2 (elevation angle dependent range error). In terms of horizontal direction AP precision (excluding b_5) the best and worst precision estimates were ±0.7″ (b_4) and ±4.4″ (b_3), respectively (both are coefficients of non-orthogonality between the horizontal circle and vertical axis). The maximum and minimum precision estimates for b_5 respectively were ±5.6 ppm and ±19.1 ppm. The elevation angle precision range was similar to that of the horizontal direction, with best and worst precision estimates of ±0.6″ (c_4, periodic error in elevation angle) and ±4.2″ (c_2, vertical circle index error), respectively. Precision estimates for all APs are indicated graphically in Figs. 8, 9 and 10.

4.3. Time series analysis

Prior to assessing whether any significant differences exist between calibration dataset APs, the significance of each AP should first be assessed. To do so, the procedure of Zhong (1997) was followed.
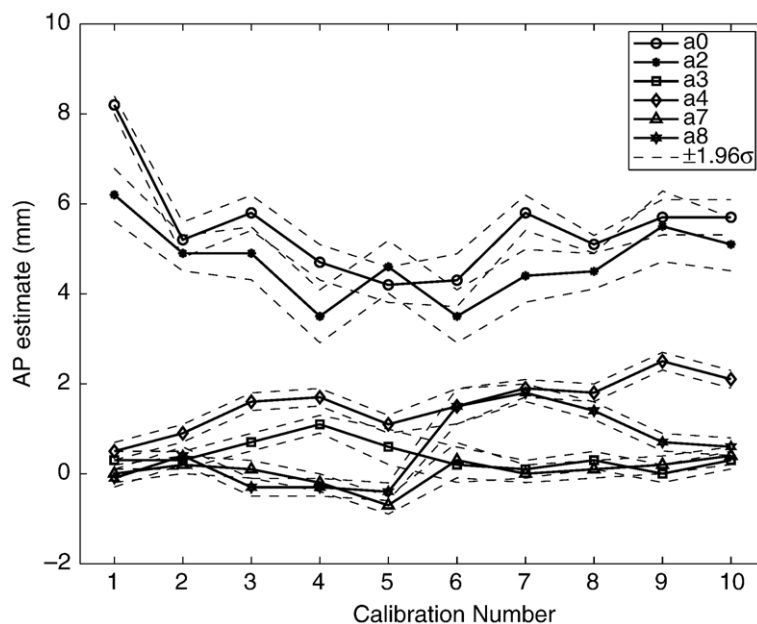

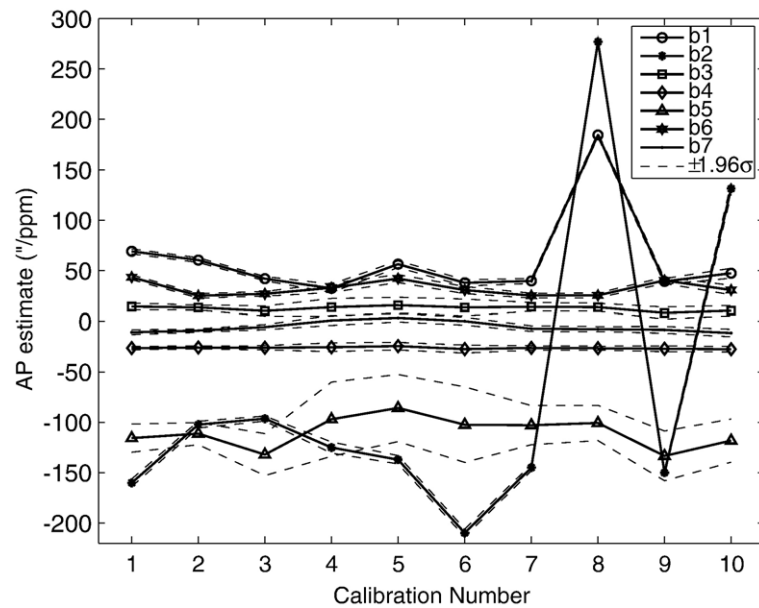Fig. 8. Range APs and 2σ confidence envelopes as a function of calibration.

Fig. 9. Horizontal direction APs and 2σ confidence envelopes as a function of calibration.

Under the null hypothesis that the expected value of an individual AP is zero, the quadratic form of the parameter normalised by the *a posteriori* variance factor, which is Fisher distributed with 1 and *r* degrees-of-freedom, was examined. The test presumes that the APs are uncorrelated with other parameters—which, as mentioned earlier, is not true for all. However, it is a practical procedure designed to

identify the optimal set of parameters (Zhong, 1997). From the 10 datasets, only four APs were identified as insignificant at the 95% confidence level: a_3 (cyclic error) 3 times; a_7 (direction-dependent range error) 7 times; b_7 3 times; and c_4 once. Parameters a_3, a_7 and c_4 are the smaller components of (orthogonal) two-term error models, so their identification as being insignificant is perhaps not surprising.
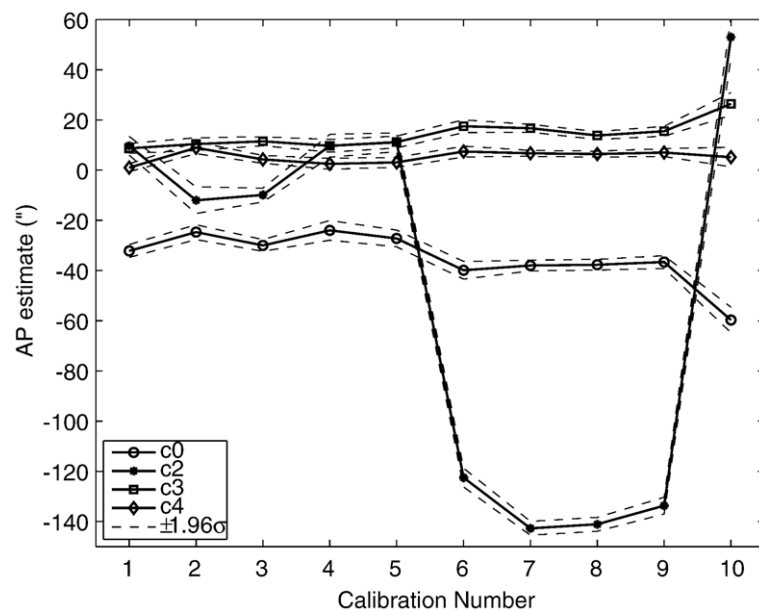

Fig. 10. Elevation angle APs and 2σ confidence envelopes as a function of calibration.

To examine whether the APs have changed significantly, the quadratic form of individual parameter differences from two calibrations – reasonably assumed to be uncorrelated – normalised by the combined *a posteriori* variance factor was examined. This statistic is Fisher distributed with 1 and r_1+r_2 degrees-of-freedom. Shortis et al. (2001) form a similar statistic as do Nasu and Anderson (1976), Jacobsen (1982) and Habib and Morgan (2005) but for the complete AP set. The results of 9 comparisons conducted at 95% confidence are given in Table 3. Figs. 8, 9 and 10 plot the additional parameters with 95% (1.96σ) error bar envelopes according to calibration number. Fig. 8 suggests that all range APs, particularly the largest ones (a_0 and a_2), are highly variable over time. This is confirmed by the number of times each was identified as being significantly different (Table 3), which ranged from a minimum of 3 for a_7 to a maximum of 6 for a_4. Fig. 8 also shows the large magnitude of a_8 after the instrument servicing between calibrations 5 and 6. Interestingly, its magnitude diminishes thereafter. Fig. 9 shows b_3 and b_4 to be very stable over time, as is b_5 despite seeming to vary quite substantially, but its units are different (ppm). The stability of these three, even after instrument servicing and shock loading, is confirmed by Table 3: neither of them is flagged as differing significantly from one

calibration to the next. The APs b_1, b_2 and b_6 exhibit more variability over time as seen in Fig. 9 and Table 3, with b_1 and b_6 each failing the statistical test in 7 cases and b_2 failing in all 9 comparisons. The graph of b_7 appears to be more stable but it does change sign and fails the test 3 times. It should be recalled, however, that calibration 8 was undertaken with some of the Faro parameters set to zero, so the corresponding changes in b_1 and b_2 were expected. The parameters c_3 and c_4 behave in a more stable manner than either of c_0 and c_2 (see Fig. 10). The latter changes sign prior to experiencing large changes after servicing (calibration 6) and shock load (calibration 10). Many APs changed as a result of the latter event.

To evaluate short-term stability, first consider datasets 4 and 5. According to the statistical test results, 7 out of 17 APs changed significantly, four of which were range parameters. The largest was a_2, which changed by 1.1 mm, but the other three differed by ≤ 0.6 mm, In terms the direction observations, b_1 changed the most: by 24″ or 1.2 mm at 10 m range and 45° elevation angle. Five APs from datasets 7 and 8 changed significantly, though two (b_1 and b_2) did so by large amounts due to the alteration of the Faro calibration parameters. No other parameters were affected on such a large scale. One of the other three that changed, a_0, did so by only 0.7 mm.

Table 3
Results from statistical testing of AP differences

	Calibration datasets compared								
	1–2	2–3	3–4	4–5	5–6	6–7	7–8	7–9	9–10
	10 December 2004–31 March 2005	31 March 2005–7 June 2005	7 June 2005–8 August 2005	8 August 2005–9 August 2005	9 August 2005–27 September 2005	27 September 2005–28 October 2005 (1)	28 October 2005 (1)–28 October 2005 (2)	28 October 2005 (1)–7 December 2005	7 December 2005–19 January 2006
a_0	×	×	×			×	×		
a_2	×		×	×	×			×	
a_3		×	×	×					×
a_4	×	×		×	×			×	×
a_7	×			×	×				
a_8	×	×			×		×	×	
b_1	×	×	×	×	×		×		×
b_2	×	×	×	×	×	×	×	×	×
b_3									
b_4									
b_5									
b_6	×		×	×	×	×		×	×
b_7		×	×			×			
c_0	×	×	×		×				×
c_2	×		×		×	×		×	×
c_3					×		×		×
c_4	×	×			×				

A '×' entry indicates a significant difference exists at 95% confidence; no entry indicates no significant difference exists.

Despite the outcomes of the statistical testing, in particular the short-term investigations, the physical significance of some of these changes is questionable given that the RMS of residuals from self-calibration was often greater than the AP change. For example, in the case of a_0 from datasets 7 and 8 captured on the same day, the RMSs of range residuals were ±1.4 mm and ±1.2 mm, roughly twice the apparent change in the AP. This testing procedure is known to suffer from several shortcomings and can be pessimistic (Habib and Morgan, 2005). (Note that it was adopted as a means to an end; examination of the reliability of such tests is not one of the aims of this work.) Thus, despite their statistical significance, it is not clear whether all these changes represent genuine physical differences due to instability in the instrument construction or a shortcoming in the testing procedure itself. What is clear, however, is that investigation into a more appropriate statistical testing procedure that measures the significance of the change in object space is required.

4.4. Outlier identification

In all calibration datasets described thus far, many outliers were observed in the range residuals that seem to exhibit a periodic behaviour as a function of range. A prime example is calibration 2 shown in Fig. 11 (Top). The apparently periodic behaviour with increasing amplitude might suggest cyclic errors caused by multiple reflections (e.g., Blug et al.,

2005). However, deeper investigation reveals this is not the case.

Inspection of the range residuals as a function of incidence angle, β, in Fig. 11 (Bottom) shows that, with only a few exceptions between 10° and 15°, the large outliers occur at incidence angles greater than about 65° or 70°. (No post-adjustment outlier removal had been performed on these data.) Interestingly, the horizontal direction and elevation angle residuals were consistently found to be independent of incidence angle. These behaviours were found for other datasets, though with varying numbers of range outliers. In related work, Ye and Borenstein (2002) report a set of experiments conducted on a 2D scanner including quantification of the effect of incidence angle at close range (i.e. 2 m). They found no significant range error for incidence angles less than 20°. However, they did find errors at higher incidence angles: a difference of up to 16 mm between ranges at 10° and 60°.

Since the evidence suggests that range is biased as a function of incidence angle, it would seem prudent to remove *a priori* any obliquely scanned points so as to minimise the number of outliers. To arrive at a threshold for excluding these points, the range residual RMS was calculated as a function of incidence angle in 5° bins from 0° to 80°, which is plotted for all 10 calibration datasets in Fig. 12. Clearly the RMS is effectively constant up to 65°, where it increases markedly. The one deviation from this trend at 77.5° was computed with only 4 data points. Thus, a
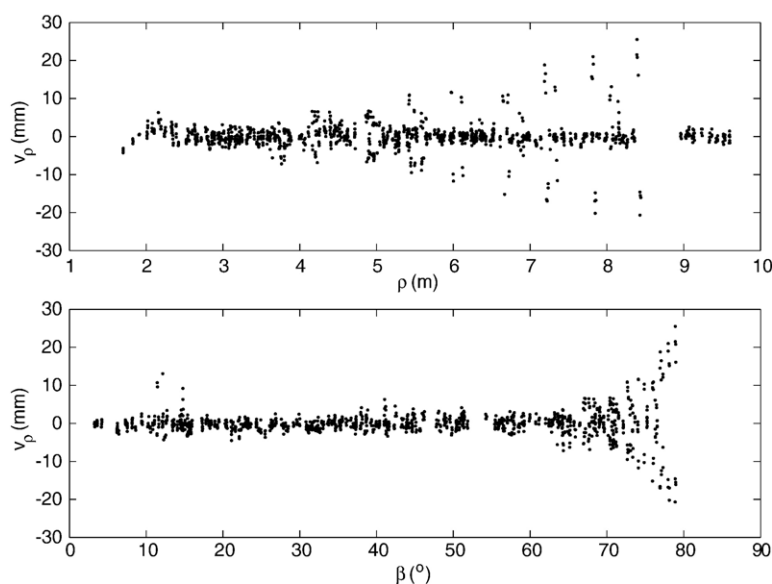

Fig. 11. Range residuals from the 31 March 2005 dataset (calibration 2). Top: as a function of range. Bottom: as a function of incidence angle.
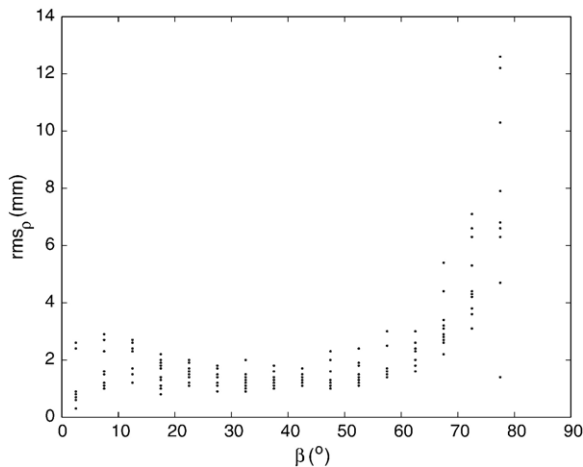
Fig. 12. Range residual RMS as a function of incidence angle for all 10 datasets.

maximum incidence angle of 65° would seem to be a logical threshold for *a priori* outlier identification and removal for this system. Exclusion of such points should not impact on the ability to estimate parameters requiring a high range of elevation angles, such as trunnion axis error. Past experience calibrating the Faro scanner has shown that high elevation angles are associated with lower (e.g., 30° to 40°) incidence angles (Lichti and Franke, 2005).

4.5. Inclinometer observations

Calibration dataset 9 was captured with the inclinometer capability enabled. To examine the effects of these additional observations, self-calibration adjustments of the dataset both with and without them were performed and compared. Analyses revealed that there were no differences between the estimated APs or their *a posteriori* precision. The RMS of the 16 orientation angle observation residuals (8 for ω; 8 for ϕ) was $\pm 0.034°$ ($\approx 2'$), somewhat higher than the manufacturer's specification but the sample size is small.

The inclinometer observations are highly controlled in the self-calibration adjustment, as indicated by their redundancy numbers of 0.87. However, they do benefit the calibration by reducing correlation between some model parameters. First, they completely de-correlate the ω and ϕ rotation angles from the APs, most notably c_0, with which in normal self-calibration they share moderate correlation coefficients of up to 0.5, and a_2, for which the correlation coefficient is up to 0.4. Second, and very interestingly, they serve to de-correlate Z_s and a_2. These parameters' correlation coefficients without inclinometer observations were as high as 0.89, but they

dropped to 0.12 when the ω and ϕ observations were added. As a consequence, though, the maximum correlation between Z_s and ω and ϕ rose from 0.50 to 0.98. Similar results were found for calibration 10, though the RMS of the 16 inclinometer residuals was considerably higher at $\pm 0.058°$ (209″). In summary, despite the seemingly relatively low precision, addition of the inclinometer observations is beneficial to the quality of the self-calibration solution in terms of reduced EO–AP correlation.

5. Conclusions

Models that include spherical co-ordinate observations and inclinometer observations have been presented for point-based terrestrial laser scanner system self-calibration. A combination of physically interpretable and empirically identified APs was found to be necessary for the system studied, the Faro 880. Though the focus is on one particular make and model of AM–CW scanner system, the mathematical models were formulated independent of instrumentation, although it is recognised that some of the APs, particularly the empirical ones, may very well be instrument dependent. Furthermore, the need for some of these may stem from the application of the manufacturer's (unpublished) correction models. It should also be noted that all additional parameters and performance metrics (e.g. accuracy estimates) are inherently coupled to the system – the instrument, the target used, as already mentioned, and this target measurement method – not just the scanner itself.

Results from 10 self-calibration experiments conducted over a 13-month period were presented. The efficacy of the method and models was demonstrated both in terms of reducing the dispersion of self-calibration residuals and through independent accuracy assessment with checkpoints. Though the percentage improvements differed in these two cases, the absolute RMSs of self-calibration residuals and co-ordinate differences were commensurate. A statistical testing procedure was employed to examine AP and, hence, instrument stability. Only three of the APs were found to be stable over the study period and significant differences were found in many APs both over the short term (hours and days) and long term (over the course of 13 months). However, it is not clear whether these are due to physical changes in the instrument or a shortcoming of the adopted statistical testing method. This finding has highlighted the need for a more appropriate statistical testing procedure.

There were two other important outcomes. First, examination of the influence of incidence angle on

rangefinder measurements led to an *a priori* outlier removal method. Second, addition of the inclinometer observations to the self-calibration was shown to be beneficial. Despite the seemingly low precision of these observables, improvement to solution strength in terms of reduced EO–AP correlation was demonstrated.

Acknowledgements

References

Abmayr, T., Dalton, G., Hätrl, F., Hines, D., Liu, R., Hirzinger, G., Frölich, C., 2005. Standardization and visualization of 2.5D scanning data and color information by inverse mapping. In: Grün, A., Kahmen, H. (Eds.), Proceedings Optical 3-D Measurement Techniques VII, Vienna, Austria, 3–5 October, 2005, vol. I, pp. 164–173.

Adams, M.D., 1999. Sensor Modelling, Design and Data Processing for Autonomous Navigation. World Scientific, Singapore.

Amiri Parian, J., Grün, A., 2005. Integrated laser scanner and intensity image calibration and accuracy assessment. The International Archives of the Photogrammetry, Remote Sensing and Spatial Information Sciences 36 (Part 3/W19), 18–23.

Blug, A., Baulig, C., Wölfelschneider, H., Höfler, H., 2005. Novel geometry for a high-speed outdoor laser scanner system. In: Grün, A., Kahmen, H. (Eds.), Proceedings Optical 3-D Measurement Techniques VII, Vienna, Austria, 3–5 October, 2005, vol. I, pp. 154–163.

Böhler, W., Bordas Vicent, M., Marbs, A., 2003. Investigating laser scanner accuracy. The International Archives of the Photogrammetry, Remote Sensing and Spatial Information Sciences 34 (Part 5/C15), 696–701.

Cooper, M.A.R., 1982. Modern Theodolites and Levels, second ed., Granada Publishing, London.

Covell, P.C., Rüeger, J.M., 1982. Multiplicity of cyclic errors in electro-optical distance meters. Survey Review 26 (203), 209–224.

Gielsdorf, F., Rietdorf, A., Gruendig, L., 2004. A concept for the calibration of terrestrial laser scanners. Proceedings FIG Working Week, Athens, Greece, 22–27 May 2004. on CD-ROM.

Habib, A., Morgan, M., 2005. Stability analysis and geometric calibration of off-the-shelf digital cameras. Photogrammetric Engineering and Remote Sensing 71 (6), 733–741.

Harvey, B.R, Rüeger, J.M., 1992. Theodolite observations and least squares. The Australian Surveyor 37 (2), 120–128.

Hebert, M., Krotkov, E., 1992. 3D measurements from imaging laser radars: how good are they? Image and Vision Computing 10 (3), 170–178.

Ingensand, H., 2006. Metrological aspects in terrestrial laser-scanning technology. Proceedings 3rd IAG/12th FIG Symposium, Baden, Austria, 22–24 May 2006. on CD-ROM.

Jacobsen, K., 1982. Attempt at obtaining the best possible accuracy in bundle block adjustment. Photogrammetria 37 (6), 219–235.

Kersten, T., Sternberg, H., Mechelke, K., Acevedo Pardo, C., 2004. Terrestrial laser scanning system Mensi GS100—accuracy tests, experiences and projects at the Hamburg University of Applied Sciences. The International Archives of the Photogrammetry, Remote Sensing and Spatial Information Sciences 34 (Part 5/W16) (on CD-ROM).

Kersten, T.P., Sternberg, H., Mechelke, K., 2005. Investigations into the accuracy behaviour of the terrestrial laser scanning system Mensi GS100. In: Grün, A., Kahmen, H. (Eds.), Proceedings Optical 3-D Measurement Techniques VII, Vienna, Austria, 3–5 October, 2005, vol. I, pp. 122–131.

Kuang, S., 1996. Geodetic Network Analysis and Optical Design: Concepts and Applications. Ann Arbor Press, Chelsea, Michigan.

Langer, D., Mettenleiter, M., Härtl, F., Fröhlich, C., 2000. Imaging radar for 3-D surveying and CAD modeling of real-world environments. International Journal of Robotics Research 19 (11), 1075–1088.

Li, W.X., Mitchell, L.D., 1995. Laser scanning system testing—errors and improvements. Measurement 16 (2), 91–101.

Lichti, D.D., Franke, J., 2005. Self-calibration of the iQsun 880 laser scanner. In: Grün, A., Kahmen, H. (Eds.), Proceedings Optical 3-D Measurement Techniques VII, Vienna, Austria, 3–5 October, 2005, vol. I, pp. 112–121.

Lichti, D.D., Licht, M.G., 2006. Experiences with terrestrial laser scanner modelling and accuracy assessment. The International Archives of the Photogrammetry, Remote Sensing and Spatial Information Sciences 36 (Part 5), 155–160.

Lichti, D.D., Stewart, M.P., Tsakiri, M., Snow, A.J., 2000. Calibration and testing of a terrestrial laser scanner. The International Archives of the Photogrammetry, Remote Sensing and Spatial Information Sciences 33 (Part B5/2), 485–492.

Lichti, D.D., Gordon, S.J., Stewart, M.P., Franke, J., Tsakiri, M., 2002. Comparison of digital photogrammetry and laser scanning. Proceedings CIPA WG 6 International Workshop on Scanning Cultural Heritage Recording, Corfu, Greece, 1–2 September 2002, pp. 39–44.

Lin, P.D., Lu, C.-H., 2005. Modeling and sensitivity analysis of laser tracking systems by skew-ray tracing method. Journal of Manufacturing Science and Engineering 127 (3), 654–662.

Nasu, M., Anderson, J.M., 1976. Statistical testing procedures applied to analytical camera calibration of non-metric systems. Photogrammetric Engineering and Remote Sensing 42 (6), 777–788.

Reshetyuk, Y., 2006. Calibration of terrestrial laser scanners for the purposes of geodetic engineering. Proceedings 3rd IAG/12th FIG Symposium, Baden, Austria, 22–24 May 2006. on CD-ROM.

Riegl, 2001. LMS-Z210 Laser Mirror Scanner Technical Documentation and Users Instructions. Riegl, Horn, Austria. 82 pp.

Rietdorf, A., Gielsdorf, F., Gruendig, L., 2003. Combination of hand measuring methods and scanning techniques for CAFM-data acquisition. Proc FIG Working Week, Paris, France, 13–17 April 2003. on CD-ROM.

Rüeger, J.M., 1990. Electronic Distance Measurement: an Introduction, third ed. Springer-Verlag, Heidelberg, Germany.

Schulz, T., Ingensand, H., 2004a. Terrestrial laser scanning—investigations and applications for high precision scanning. Proceedings FIG Working Week, Athens, Greece, 22–27 May 2004. on CD-ROM.

Schulz, T., Ingensand, H., 2004b. Influencing variables, precision and accuracy of terrestrial laser scanners. Proceedings of IGEO 2004: 3rd International Conference on Engineering Surveying, Bratislava, Slovakia, 11–13 November 2004. on CD-ROM.

Shortis, M.R., Ogleby, C.L., Robson, S., Karalis, E.M., Beyer, H., 2001. Calibration modelling and stability testing for the Kodak

DC200 series digital still camera. Proceedings Videometrics and Optical Methods for 3D Shape Measurement, San Jose, CA, USA, 22–23 January 2001. SPIE, vol. 4309, pp. 148–153.

Spiess, S., Vincze, M., Ayomlou, M., 1998. On the calibration of a 6-D laser tracking system for dynamic robot measurements. IEEE Transactions on Instrumentation and Measurement 47 (1), 270–274.

University College London (UCL), 2001a. Best Practice for Non-Contacting CMMs. 20 p. http://www.ge.ucl.ac.uk/research/industrial_metrology_close_range_photogrammetry_and_laser_scanning/nmsp_for_length_metrology (accessed October 16, 2006).

University College London (UCL), 2001b. Modelling for Non-Contact CMMs. 48 pp. Available at http://www.ge.ucl.ac.uk/research/industrial_metrology_close_range_photogrammetry_and_laser_scanning/nmsp_for_length_metrology (accessed October 16, 2006).

Witte, B., Schwarz, W., 1982. Calibration of electro-optical range-finders—experience gained and general remarks relative to calibration. Surveying and Mapping 42 (2), 151–162.

Ye, C., Borenstein, J., 2002. Characterization of a 2-D laser scanner for mobile robot obstacle negotiation. Proceedings of the IEEE International Conference on Robotics and Automation, Washington, DC, May 2002, pp. 2512–2518.

Zhong, D., 1997. Robust estimation and optimal selection of polynomial parameters for the interpolation of GPS-geoid heights. Journal of Geodesy 71 (9), 552–561.

Zhuang, H., Roth, Z.S., 1995. Modeling gimbal axis misalignments and mirror centre offset in a single-beam laser tracking measurement system. The International Journal of Robotics Research 14 (3), 211–224.